ORNL/TM-2020/1609

MICROSTRUCTURE AND STRENGTH OF A THICK-SECTION GAS-TUNGSTEN ARC WELD IN CAST HAYNES® 282® ALLOY

Michael Santella
Xiang (Frank) Chen
Jason Rausch
Jonathan Salkin
Philip Maziasz

September 2020

OAK RIDGE NATIONAL LABORATORY
MANAGED BY UT-BATTELLE FOR THE US DEPARTMENT OF ENERGY

ORNL/TM-2020/1609

Materials Science and Technology Division

MICROSTRUCTURE AND STRENGTH OF A THICK-SECTION GAS-TUNGSTEN ARC WELD IN CAST HAYNES® 282® ALLOY

Michael Santella
Xiang (Frank) Chen
Jason Rausch
Jonathan Salkin
Philip Maziasz

Date Published: September 2020

Prepared by
OAK RIDGE NATIONAL LABORATORY
Oak Ridge, TN 37831-6283
managed by
UT-BATTELLE, LLC
for the
US DEPARTMENT OF ENERGY
under contract DE-AC05-00OR22725

CONTENTS

ABSTRACT

A 50-mm deep gas tungsten arc weld was made with matching filler metal in cast Haynes 282 alloy. The narrow gap joint was filled with 104 weld beads. The weld deposit was of high quality with no visible indications of physical defects. The weld heat-affected zone was characterized by microcracking and localized recrystallization. Hardness testing showed that a softened region in the as-welded heat-affected zone was nearly eliminated by post-weld heat treatment. Tensile testing up to 816°C showed that cross-weld specimen strengths were about 80% of the yield strength of the original cast base metal. The rupture strengths of cross-weld specimens are within 20% of wrought base metal reference data.

1. INTRODUCTION

It seems likely that for the foreseeable future coal will remain important globally as a fuel for utility power generation. It is abundant and remains cost-competitive relative to other fossil fuels [1]. However, its negative impacts on the environment are well established. Among other issues, its combustion produces undesirable atmospheric concentrations of SO_X, NO_X, and CO_2, and large quantities of ash [2,3]. While the long-term outlook for using coal in power generation may be uncertain, there is interest in technologies that can minimize the negative impacts. One strategy for this involves increasing the operating temperature and pressure in coal-fired utility boilers to increase their efficiencies and reduce emissions [4].

The ability to increase the operational conditions of utility boiler systems will depend on the availability or development of higher temperature alloys than are typically used in more conventional systems [4,5,6]. Critical components such as heavy-wall pipe and headers, tubing, and large land-based turbine parts will require the use of nickel-based alloys with good high-temperature strength and fabricability. One alloy that has emerged as a likely candidate for some of these applications is Haynes 282 (UNS N07208) [7,8]. Although Haynes 282 was originally targeted for applications where it would be used in relatively thinner gages [9,10], it is also being evaluated for thick-walled wrought and cast applications.

The primary objective of the work presented here was to make and get an initial assessment of the stress-rupture properties of a 50-mm-deep narrow-gap gas-tungsten arc weld (GTAW) in a section of Haynes 282 casting that was originally 100 mm thick. A sound weld was produced with good properties. Detailed characterization of microstructure was beyond the scope of work, but some was necessarily done in attempting to reconcile observed behaviors.

2. EXPERIMENTAL DETAILS

The Haynes 282 material for this weld was a hollow cylindrical ring section cut from a large, prototype valve body casting weighing approximately 7,700 kg [8]. The ring section was homogenized, spending 68 h between 1190-1225°C, and given the recommended two-step strengthening heat treatment of 2 h at 1010°C followed by 8 h at 788°C [11]. Figure 1 is a photograph of the ring section, as it was supplied for welding. The size of the ring was approximately 355-mm-OD x 100-mm-wall x 152-mm-ring height. The ring was finally cut into two 180° arc sections, one of which was used for welding. This was done to provide enough material for various test specimens while limiting the weld length, and, therefore, the total weight of welding wire needed to complete the desired weld.

Because extensive machining was required to prepare a joint for welding, the 180° arc section was given another heat treatment of 1 hour at 1150°C to reduce its hardness. The top and bottom surfaces were then machined parallel. The EDM wire cutting process was used to remove excess from the OD and ID and to accurately cut the arc of the OD and ID so they were concentric to each other. After this, EDM was then used to bisect the 180° arc section along its circumference to produce two identical half-ring pieces. The two half-rings were then tack-welded together to form a complete 360° ring that was mounted onto a vertical lathe for machining onto the ring face of the narrow gap joint detail shown as Figure 2. Finally, this assembly was reconfigured as two half-rings and set-up for welding.

Positioning the half-ring assembly for welding involved rigidly attaching it to a length of thick-walled carbon steel pipe with gussets of Inconel 625 plate, Figure 3. The carbon steel pipe had been weld-overlaid with Inconel 617 and machined to mate its OD to the ID of the half-ring assembly.

The welding was done with the gas tungsten arc process using a 3-mm-diameter rotating tungsten electrode. The torch was held in a fixed, top-dead-center, flat welding position as the fixtured assembly was rotated beneath it. A cold wire feed was used with 1.14-mm-diameter wire (Haynes International, heat no. 2082-5-8366). The shielding gas was a 50/50 mixture of Ar + He. A total of 104 welding passes was used to complete the weld.

After welding was completed and the weldment was detached from fixturing, cross-section slices were EDM cut from six locations along the weld length with two slices being near its center. The two centrally-located slices were used for metallographic analyses and hardness testing. One of the slices was kept in the as-welded condition. The second slice and 30 cross-weld rod blanks were given a final strengthening heat treatment of 2 h at 1010°C followed by 8 h at 788°C. The rod blanks were machined into cross-weld test specimens having gage dimensions of 57.15-mm length x 6.35-mm diameter. These were used for both tension and stress-rupture testing. The ORNL internal designation for this specimen is SK-55-B2. The design is consistent with the small size specimen dimensions specified by ASTM E8.

More detailed descriptions of the various heat treatments, machining, fixturing, and welding are presented in Appendices A and B.

Figure 1: Ring section of Haynes 282 alloy after homogenization and strengthening heat treatment

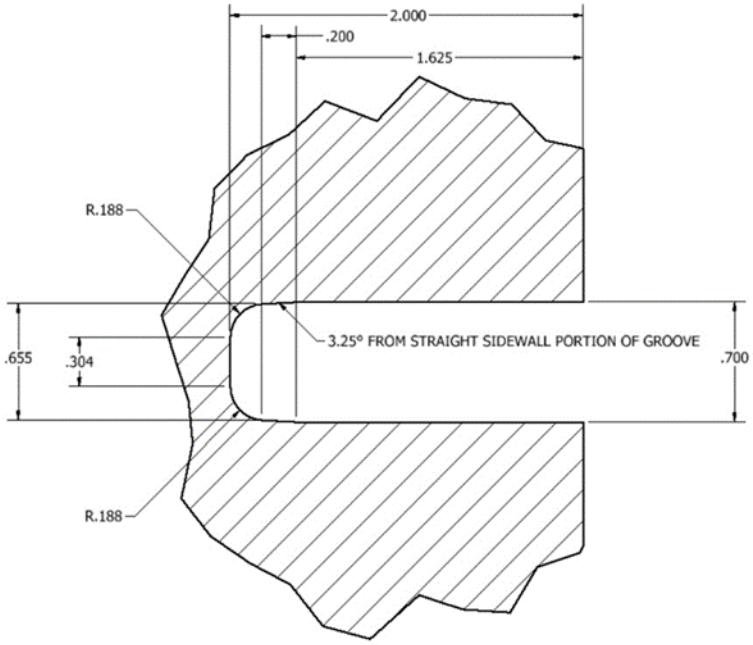

Figure 2: Weld joint machining details (units in inches)

Figure 3: Photograph showing the cast 282 half-ring sections set-up for welding after mating to the weld-overlaid carbon steel pipe but before gusset attachment

3. RESULTS AND DISCUSSION

Chemical analysis results for the cast base metal and a specimen cut from the actual weld deposit are provided in Table 1 where they are compared to the UNS N07208 chemistry specification. The chemistries of both the base metal and the weld deposit agree well with the standard.

Table 1: Chemical analysis results in wt% with Ni balance

Element	Base Metal	Weld Deposit	UNS N07208
Al	1.44	1.54	1.38-1.65
B	0.008	0.003	0.003-0.010
C	0.07	0.05	0.04-0.08
Co	10.06	10.2	9.0-11.0
Cr	19.2	19.28	18.5-20.5
Cu	0.01	0.01	0.1 max
Fe	0.46	0.75	1.5 max
Mn	0.04	0.06	0.3 max
Mo	8.28	8.41	8.0-9.0
Nb	0.05	0.04	0.2 max
P	0.004	0.005	0.015 max
S	0.002	0.001	0.015 max
Si	0.17	0.07	0.15 max
Ti	2.31	2.14	1.90-2.30
Zr	0.01	<0.01	0.020 max
O	<0.01	0.01	---
N	0.01	0.01	---

Visual examination of the six cross-weld slices found that relatively large defects were distributed throughout the cast base metal. Liquid-dye-penetrant examination revealed many smaller defects as well. Examples of the situation relative to casting defects are also available in Appendices A and B.

3.1 MICROSTRUCTURES

3.1.1 Base Metal Results

The microstructures of the cast base metal, weld deposit, and weld heat-affected zone were characterized only on metallographically prepared specimens. This was done both with light-optical microscopy and scanning electron microscopy.

The cast base metal microstructure was characterized by a large average grain size. No attempt was made to measure grain size, but grains exceeding several millimeters in major dimension could be seen on smooth, cut, or machined surfaces without the aid of magnification. Optical micrographs showing second phases precipitated on grain boundaries are shown in Figure 4 and Figure 5. Grain boundaries were outlined by second-phase particles. Judging from their shape and contrast, the particles represent multiple phases. The relative fractions of the various particles were variable throughout the microstructure. Comparison of Figure 4 and Figure 5. shows the microstructure after the strengthening heat treatment was visually identical to that of the solution treated metal.

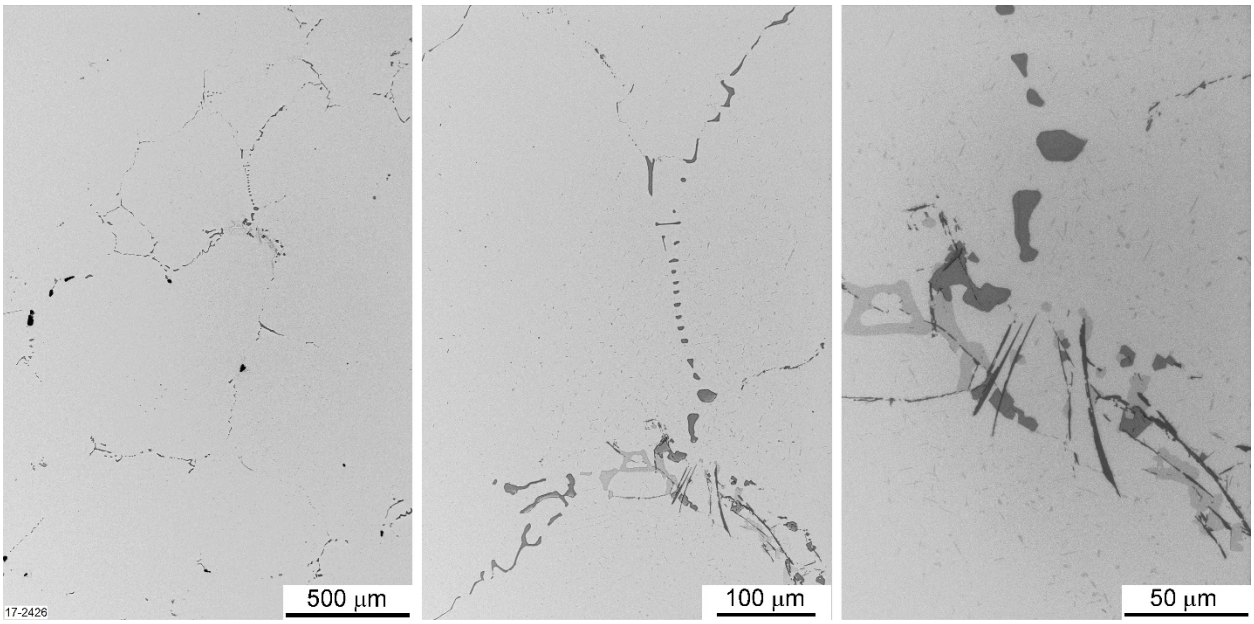

Figure 4: Optical micrographs showing general features of cast microstructure after solution treatment

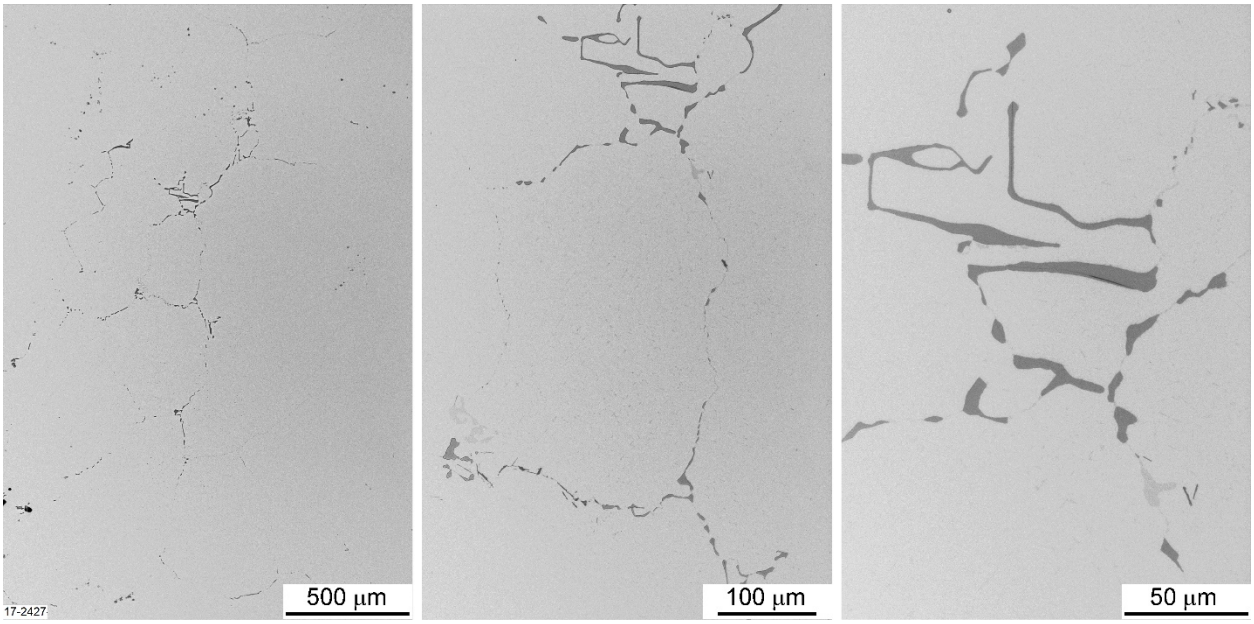

Figure 5: Optical micrographs showing general features of cast microstructure after post-weld strengthening heat treatment

The particles illustrated by Figure 6 were found randomly distributed throughout the base metal microstructure regardless of heat treatment. They had roughly geometrical shapes, and many of them were found in the matrix rather than on grain boundaries. The EDS mapping showed that their cores consisted primarily of Ti and N surrounded by rims also enriched in C and Mo. The size of these particles was often in the range of many microns in major dimension. Many of the larger particles contained cracks as Figure 6 also shows. Other small, submicron particles shown in Figure 6 were enriched in either Al, Cr, or Mo.

The particles found on grain boundaries and in interdendritic regions are highlighted by Figure 7 and Figure 8. The large, irregularly shaped particle in Figure 7, found on a grain boundary, is composed primarily of C, N, Mo and Ti. The uniform contrast of the particle suggests its chemical composition also is uniform. Cracks in the particle are also visible. The large particle is surrounded by numerous smaller, submicron-size particles. The EDS mapping indicates some of these are enriched with Al. The mapping results coupled with the bright contrast in the SEM image confirms that many of the small particles are enriched with Mo. A group of submicron particles in the matrix below the large particle is enriched in Cr.

A length of grain boundary from a different region in the heat-treated casting is shown in Figure 8. A distinctive feature at this location is the large particle of white contrast. The EDS mapping indicates it is composed mainly of Mo and Si with smaller concentrations of C and Cr. Other smaller particles both along the grain boundary and in the matrix appear to have the same composition because of their bright contrast. The two other large particles on the grain boundary are enriched in C, N, Mo, and Ti, and, judging from contrast, they have cores and rims of differing chemical composition. This is similar to those shown in Figure 6, except that their contrast characteristics are reversed with cores that are brighter than their rims. Rod-shaped particles enriched in Mo and Ti also occur in the matrix at this location. The dark contrast associated with these is like that of the dark rims around the larger particles on the grain boundary.

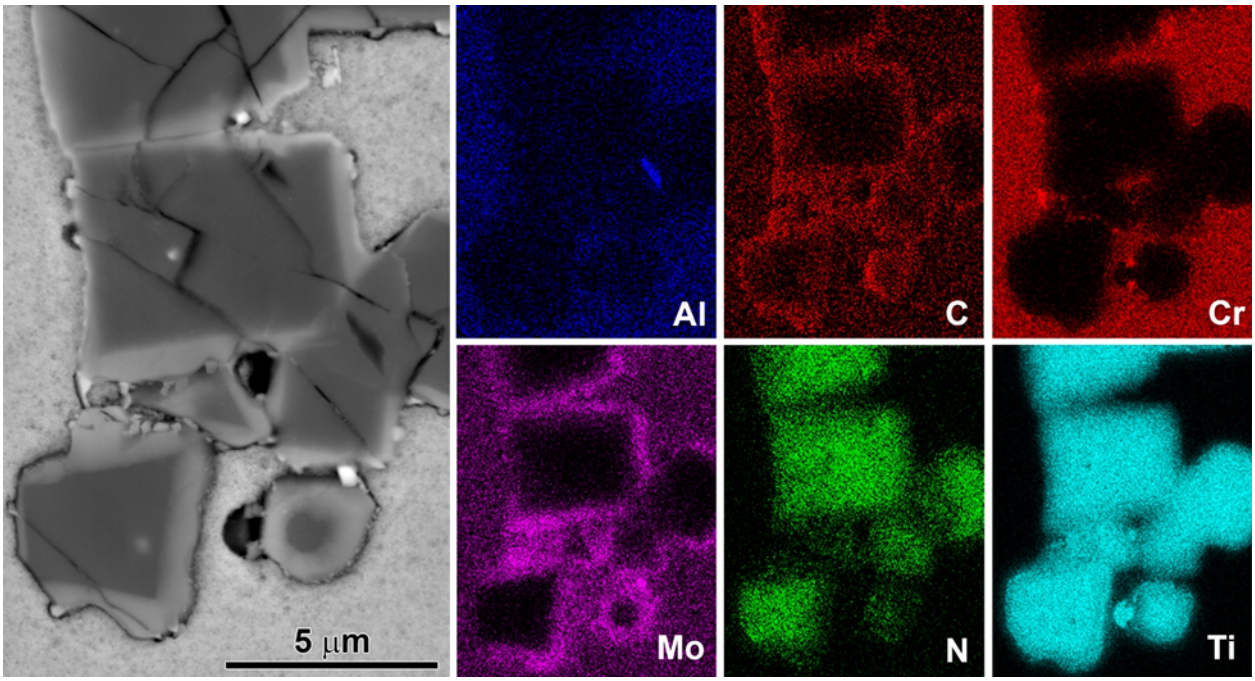

Figure 6: SEM micrograph showing details of isolated second phase particles after strengthening heat treatment

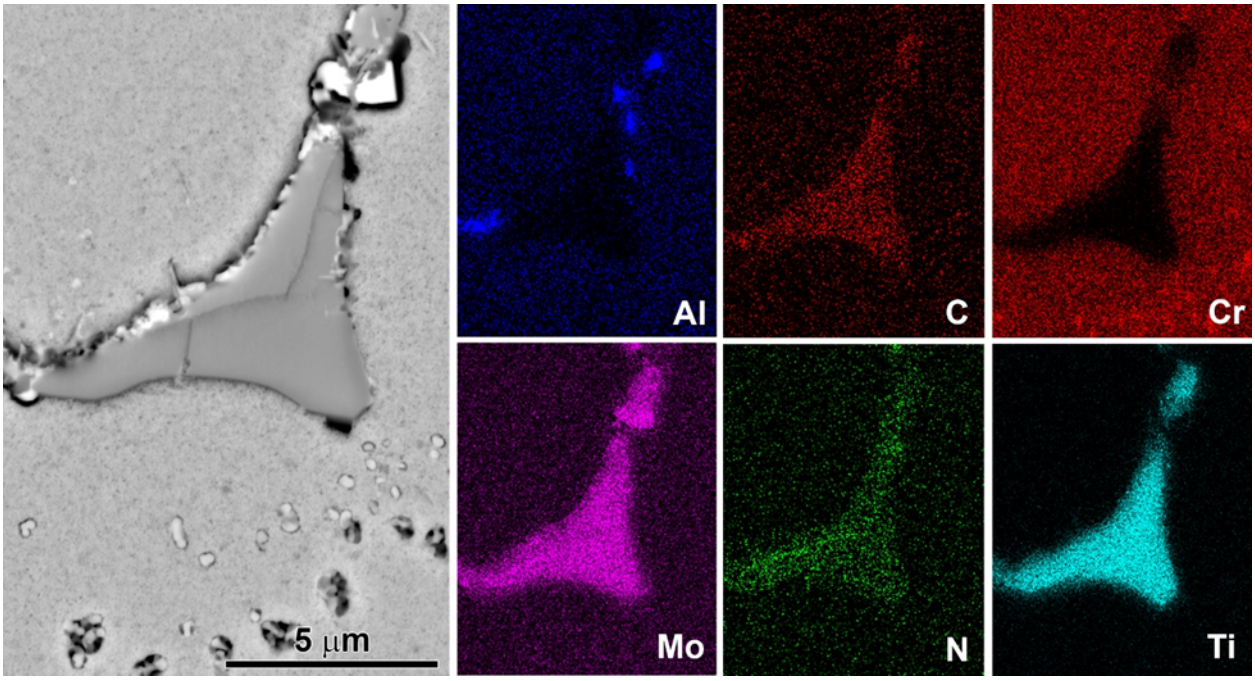

Figure 7: SEM micrograph showing second phase particles on grain boundary after strengthening heat treatment

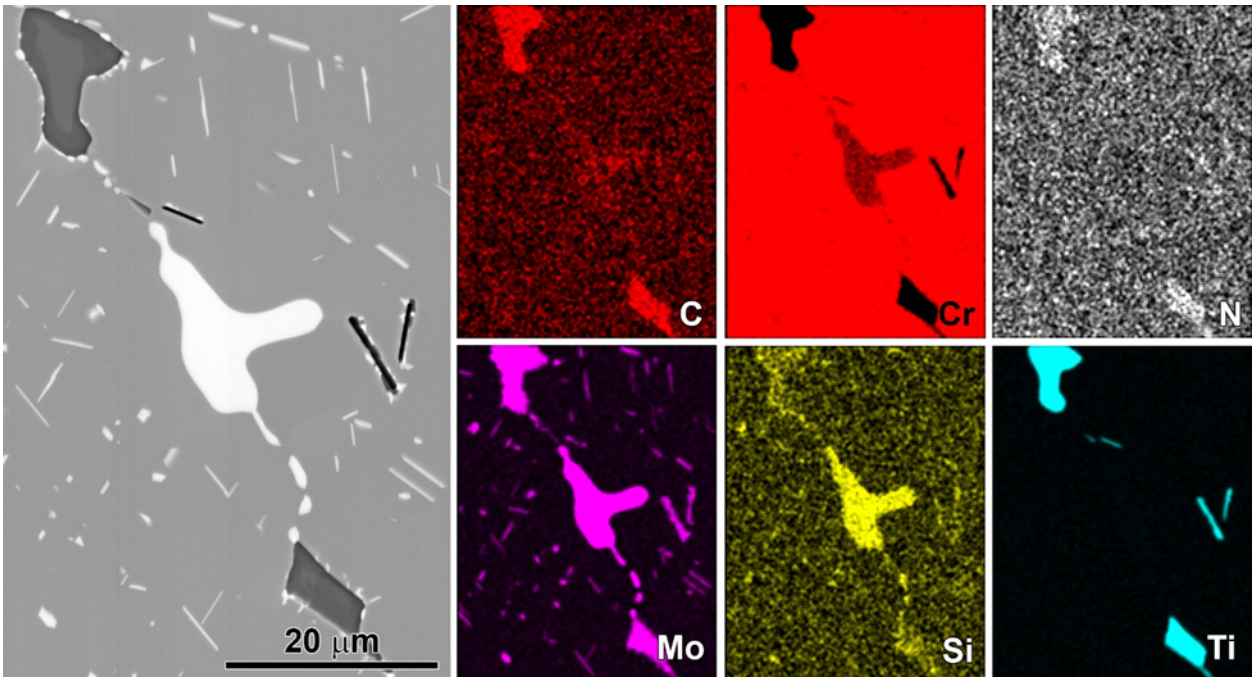

Figure 8: SEM micrograph showing second phase particles on grain boundary after strengthening heat treatment

3.1.2 Base Metal Discussion

By supplementing the metallographic observations with thermodynamic calculations most of the second phase particles in the base metal were identified with reasonable confidence. The results of calculating the variation of equilibrium second phases with temperature are shown as Figure 9 [12] where the fcc matrix

is omitted to highlight the minor phases. Also omitted is γ′, which has a calculated solvus of 998°C, and μ, with a calculated solvus of 757°C. The γ′ is omitted because it was not directly observed, and there is no reason to expect its presence deviates from expected behavior [10,13]. The μ was omitted because its formation is not expected without long time aging [14]. Furthermore, there are no published accounts of significant μ formation in Haynes 282. Also highlighted in Figure 9 is the calculated solidus of 1261°C. Considering the extensive heat treatments the casting received before welding, consisting of homogenization, the strengthening heat treatment, and solution treatment, it was expected that the casting microstructure was better represented by equilibrium conditions rather than those of a Scheil non-equilibrium solidification analysis. Scheil analyses with and without back diffusion, however, were also done.

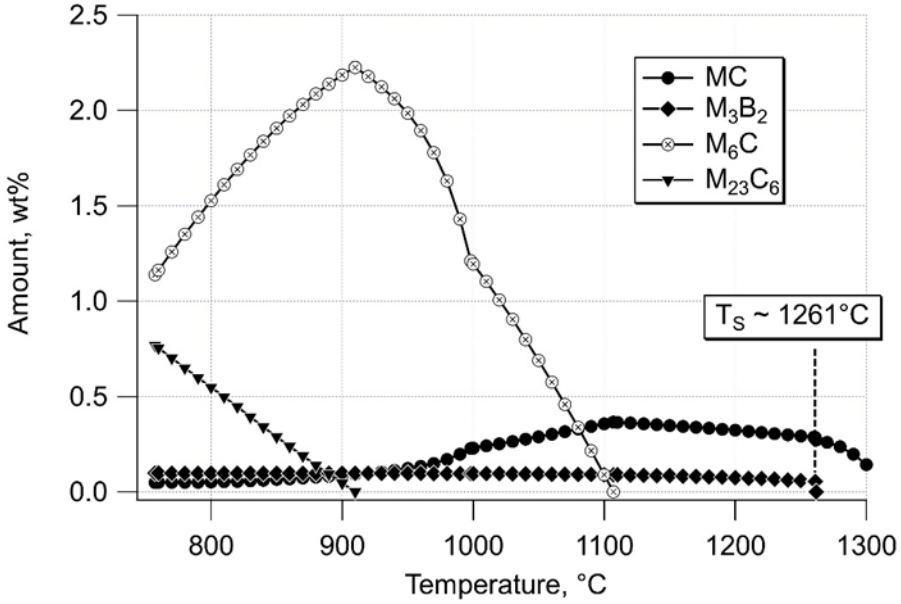

Figure 9: Calculated variation of equilibrium phases with temperature

Figure 9 indicates that an MC phase is stable above the solidus. If it formed in the liquid phase its shape would be relatively unconstrained by surface energy considerations, and it would tend to appear in areas that were last to solidify as well as being more generally distributed throughout the base metal. These features along with the EDS results are consistent with identifying the large particles shown in Figure 6 as cubic TiN. Other works on cast 282 [15,16] also show that both TiN and cored, irregularly-shaped MC particles are commonly observed. The calculated equilibrium composition of MC phase is presented in Figure 10. This result indicates that above the 1261°C solidus nearly pure TiN is the most likely form of MC phase. Below the solidus, the MC phase tends to become increasingly enriched in C until higher N concentrations are more stable once again at temperatures below about 750°C. Figure 9 also predicts that the amount of MC phase slightly increases with decreasing temperature between the solidus and the solvus of M_6C. The formation of thin C-enriched rims on the primary TiN particles is consistent with this predicted behavior. Although it is not captured by the thermodynamic analysis, enrichment of the MC phase with C appears also associated with enrichment of Mo. Some of the submicron-sized particles in Figure 7 are likely Mo_6C and $Cr_{23}C_6$ as discussed in detail by Yang et al. [16]. Small Al-rich particles inside TiN, like Figure 7 shows, were also found by Matysiak et al [15]. Those were assumed to be oxides on which the nitride nucleated.

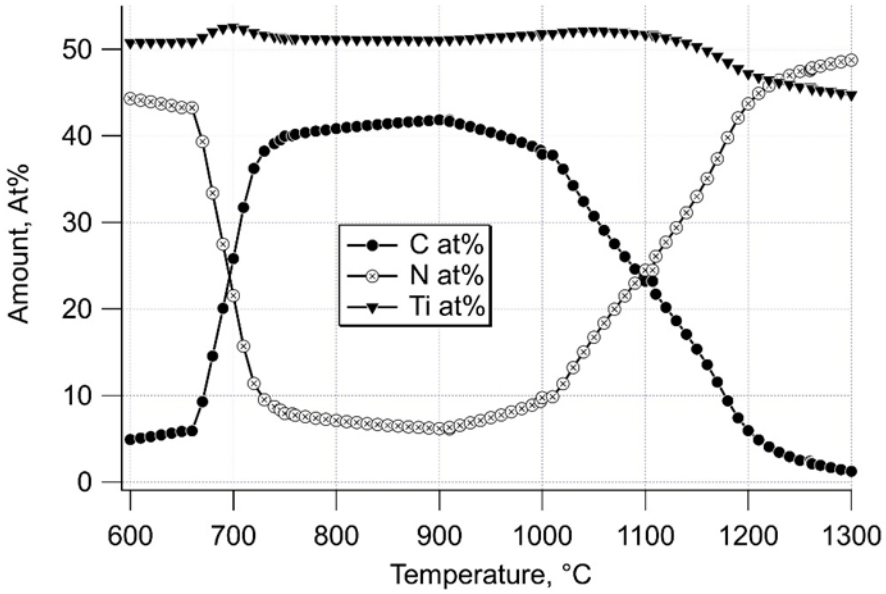

Figure 10: Calculated equilibrium composition of MC phase

Most of the large second-phase particles like those shown in Figure 6, Figure 7, and Figure 8 are MC phase. These have variable chemical composition of (Mo,Ti)(C,N) and formed both on grain boundaries and interdendritically. Both Matysiak et al [15] and Yang et al [16] confirmed by diffraction that these types of particles with variable chemical composition have the fcc structure expected of an MC-type phase. The large particle in Figure 7 is surrounded by many smaller particles in the matrix. Many of those at its interface with the matrix are likely to be M_6C [16]. Presumably, the small Al-rich particles highlighted in Figure 7 are either Al-oxides or Al-nitrides. The group of small Cr-rich particles in Figure 7 must be $M_{23}C_6$ that formed during the final strengthening heat treatment at 788°C.

According to both their bright contrast and the EDS results, the large particle in the center of Figure 8 and many of the surrounding smaller ones are clearly enriched with Mo. Both the large particle and some of the smaller ones also contain a significant concentration of Si along with small amounts of C, N, and Cr. Phases composed of these elements were not predicted by the thermodynamic analysis. Neither has this type of phase been reported in other studies of Haynes 282. Without more accurate composition and crystallographic information, it is impossible to identify this phase. Large MC particles are also found at this section of grain boundary, but in this case their contrast is the reverse of those shown in Figure 6. A possible explanation for this is that they were being depleted of C due to the formation of other carbide phases. This would raise the N concentration around the periphery of the MC particles, altering their contrast in imaging. This behavior would be consistent with Figure 10.

Although the occurrence of borides is predicted, Figure 9, none could be specifically identified during any of the characterization. No borides were reported in the works of either Matysiak et al [15] or Yang et al [16] on cast Haynes 282. On the other hand, M_5B_3 has been identified in Haynes 282 and linked to the heat-affected zone cracking of welds [17].

3.1.3 Heat-Affected Zone Results

The heat-affected zone microstructure of solution treated base metal, Figure 11(a), was characterized by a distinct region of light etching adjacent to the weld fusion line. Because the fusion line establishes a temperature at the solidus, the near heat-affected zone, i.e., that region of the heat-affected zone

immediately adjacent to the fusion line, correlates with regions experiencing excursions to the highest temperatures during welding. While residence times at the high temperatures will be relatively brief, additional dissolution of second phases, for instance, will be expected. As distance from the fusion line increases into the base metal, the peak temperatures experienced will decrease. In contrast to the near regions, metal further away from the fusion line can actually experience precipitation of second phases. The differences in the response of base metal to the peak temperatures causes the variation in etching response. At the location of Figure 11(a) there are no indications of significant defects in the near heat-affected zone. However, there are many cracks just beyond the light-etching region in the base metal.

Figure 11(b) shows the microstructure of a similar heat-affected zone region after the post-weld strengthening heat treatment. To varying degrees, regions of recrystallization in the near heat-affected zone, like that shown in Figure 11(b), were distributed along the periphery of the weld. These were typically adjacent to the fusion line. Although cracks were also found at this location, they generally did not intersect the fusion line, but tended to occur a short distance from it.

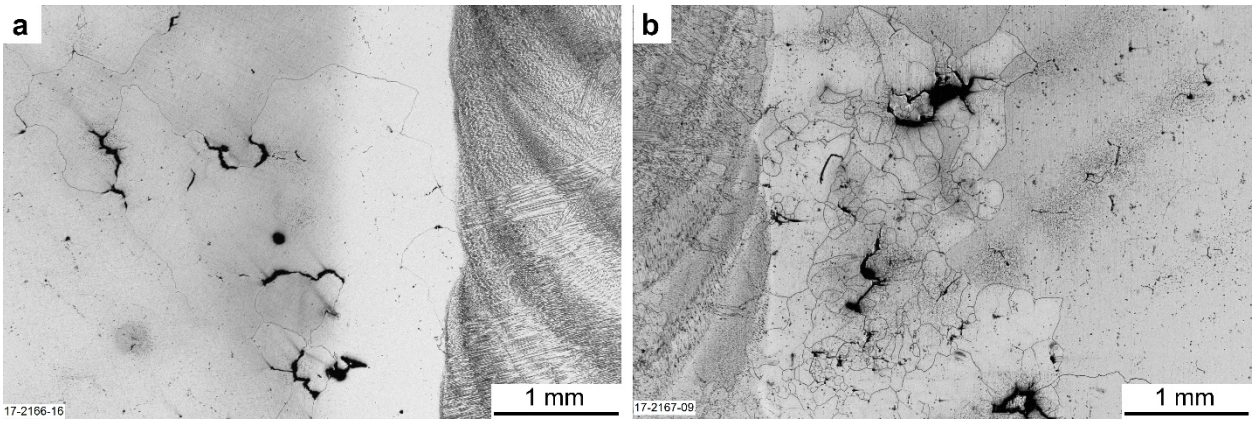

Figure 11: Optical micrographs showing weld heat-affected zone microstructure of solution treated base metal (a) and after post-weld strengthening heat treatment (b)

An example of a feature found in the heat-affected zone is illustrated with Figure 12 and Figure 13. The overall shape of the feature is similar to the large MC particle shown in Figure 7, but instead of being an intact particle it is a crack surrounded by phases of more complex morphologies. The EDS mapping was inconclusive about the C distribution, but spot analyses confirmed that locations such as the location labeled 3 on the image are the (Mo,Ti)(C,N) found throughout the cast microstructure. The bright contrast features labeled 1 appear to be individual particles that are primarily elevated in Mo and Cr. This also was confirmed by spot analysis. The region labeled 2 in the image appears composed of more than one phase. It is elevated in Mo, Ti, and N. Other particles that may be Al-nitride or Al-oxide are also visible. The overall appearance is suggestive of the transformation or reaction of a large MC particle into various product phases.

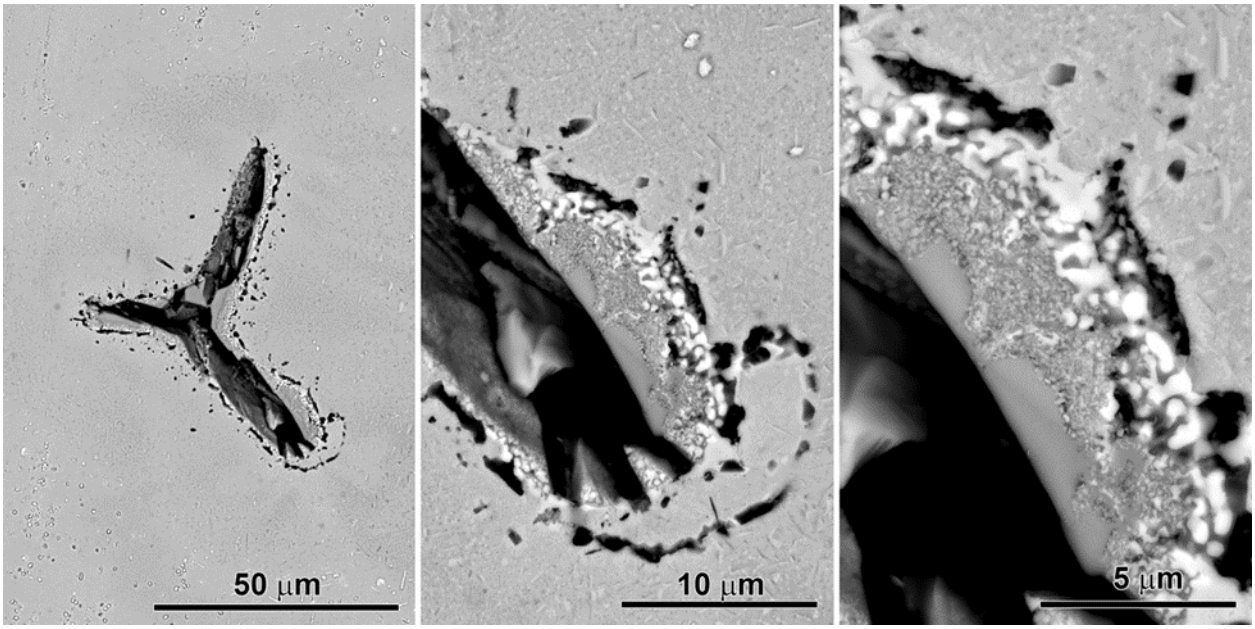

Figure 12: SEM micrograph of a second-phase particle in the weld heat-affected zone after post-weld strengthening heat treatment

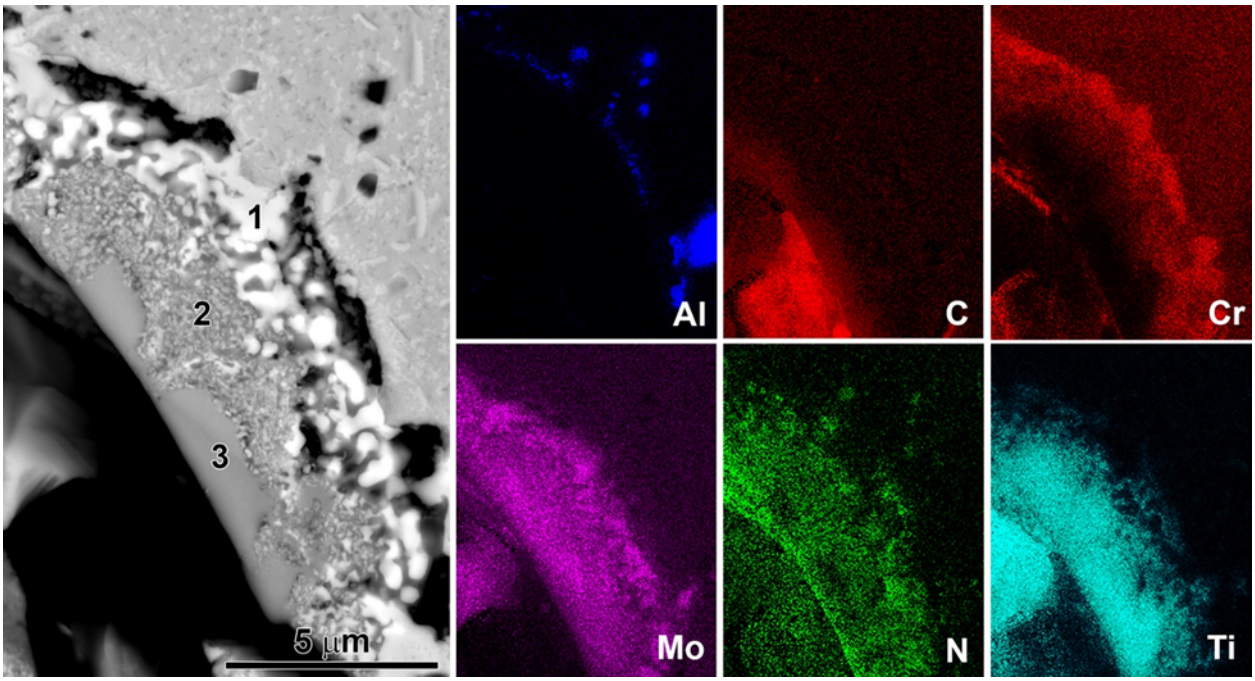

Figure 13: SEM micrograph of second-phase particle including EDS chemical composition maps

3.1.4 Heat-Affected Zone Discussion

To reiterate, this cast 282 was homogenized and then given its strengthening heat treatment. To facilitate machining the weld groove details, it was subsequently solution treated at 1150°C. After machining, it was welded and finally given a second iteration of the strengthening heat treatment. The driving force for the recrystallization illustrated by Figure 11(b) must have resulted from local surface deformation

associated with the machining. It is clear that the welding operation did not induce recrystallization, Figure 11(a). The recrystallization must have initiated during heating to and holding at 1010°C, the first step of the second strengthening heat treatment. Whether this can be a source of concern for mechanical behavior will need further evaluation. In any event, it is likely that machining operations can be modified to minimize or eliminate conditions favorable to promoting recrystallization.

With regard to cracking phenomena, both strain-age cracking and heat affected zone cracking are concerns when welding precipitation strengthened alloys like Haynes 282. The resistance of Haynes 282 to strain-age cracking is considered good [10]. On the other hand, the kinetics of the precipitation of γ′ and strengthening carbides during cooling is relatively fast [18,19]. This means that in solution treated metal, strength will likely increase and ductility will decrease for temperature excursions below the γ′ solvus. Additionally, large grain size, as is present in this Haynes 282 casting, reduces ductility under simulated welding conditions [18]. Large castings such as this one will also cool relatively slowly after welding. Both of these conditions will superimpose on any effects of precipitation kinetics and contribute to a strain-aging response.

Considering this rationale, the optical micrograph after welding the solution-treated casting, Figure 11(a) illustrates a situation that could be identified as strain-age cracking. The heat-affected zone adjacent to the fusion line at this location is free of visible defects. The peak temperatures in this region would have been high, approaching the solidus, but cooling rates would also be relatively high. These conditions are not conducive to precipitation of strengthening phases. With increasing distance from the weld fusion line, both the peak temperatures and cooling rates will progressively decrease. In a zone of moderate distance from the fusion line, peak temperatures would be below the γ′ solvus and residence time there could be long enough for significant precipitation. These regions would be susceptible to strain-age cracking, so the microstructure highlighted by Figure 11(a) is consistent with this behavior.

In contrast to strain age cracking, heat-affected zone cracks are typically associated with higher temperature phenomena. These tend to form on grain boundaries that either intersect the fusion line of the weld deposit or they are close to it. They are most often associated with high temperature ductility and strength characteristics, or liquation events that produce liquid films along grain boundaries [20]. In evaluating Haynes 282, Andersson et al. [18] concluded that hot ductility of the wrought metal was excellent, especially when compared to Waspaloy, another γ′-strengthened alloy that shares the same chemical composition space. Their work also showed that hot ductility was reduced by large grain size. The larger grains were associated with an increased tendency for liquation along grain boundaries during short-time, high-temperature excursions like would occur during welding. The liquation was attributed to eutectic formation that correlated with reductions in ductility and strength in the Haynes 282. A similar study [17,21] on wrought Haynes 282 found that reduced high-temperature ductility correlated with the liquation of M_5B_3 particles on grain boundaries. The effect of the particles at reducing ductility was magnified with increased grain size. There are no similar published accounts of the hot ductility behavior of cast Haynes 282.

Rapid dissolution of borides and carbides on grain boundaries is a plausible source of liquation in Haynes 282. This can be visualized with Figure 14 where the thermodynamic predictions from Figure 9 are replotted to highlight the M_3B_2 and MC phases. Below the 1261°C solidus, the amount of M_3B_2 continuously increases. Consequently, metal that experienced heat treatments below the solidus would likely contain an amount of M_3B_2 higher than the amount stable at the solidus. When metal with the higher amount of M_3B_2 was heated to the solidus during welding, for instance, an amount of M_3B_2 higher than what existed at the solidus would begin rapidly dissolving. The shaded region in Figure 14 represents this amount. The dissolution of any excess amounts of M_3B_2 that exist on grain boundaries will increase the local concentrations of B which is a powerful melting point depressant in Ni. A plausible result of this

is the occurrence of liquid films at low temperatures relative to the solidus and an increased tendency for heat-affected zone cracking. A similar situation exists for MC phase although its behavior is somewhat more complicated because of the formation of M_6C below about 1110°C. Rapid dissolution of MC could cause locally elevated concentrations of Ti, another powerful melting-point depressant in Ni.

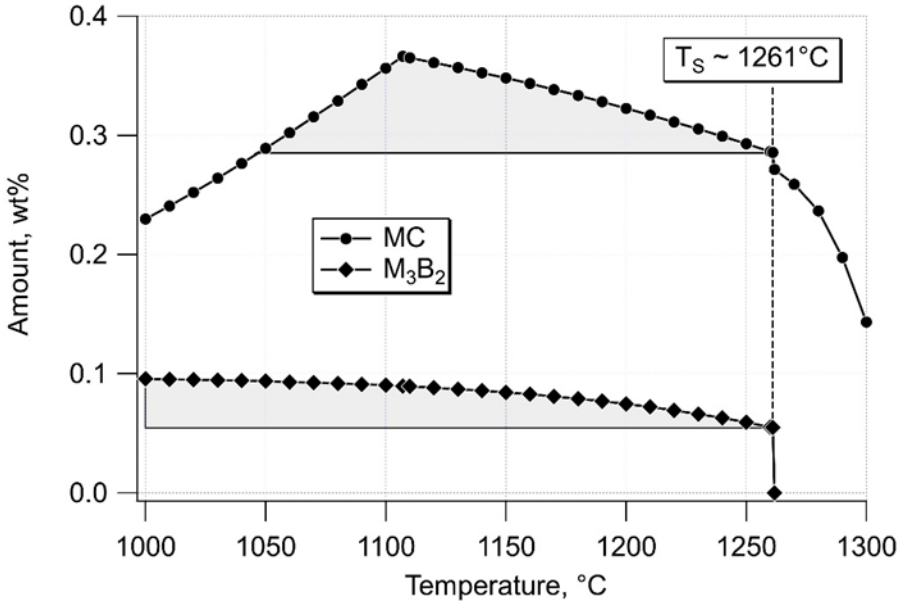

Figure 14: Calculated variations of the amounts of MC and M_3B_2 phases

Other welding studies of Haynes 282 show that both wrought and cast metal can exhibit heat-affected zone cracking [8,21]. The cracking of laser-welded wrought metal was associated with liquation of M_5B_3 particles [17] that were subsequently identified as Mo_5B_3 [22]. The heat-affected zone cracking observed in the previous work on welding cast Haynes 282 was not investigated [8].

Often the probable source of heat-affected zone cracking can be established by metallographic examinations. Many of the heat-affected zone cracks like shown in Figure 11(b) either intersected the fusion boundary between base metal and weld metal or were close to it. It was not possible, however, to determine unequivocally that any phases indicative of liquation occurred at these crack surfaces. On the other hand, cracks like that shown as Figure 12 were found at various locations in the heat-affected zone. The evidence from Figure 12 and Figure 13 suggests that this crack could have resulted from liquation of a large MC particle and that reactions with nearby particles contributed to the event. Based on the foregoing discussion, it seems prudent to be concerned about heat-affected zone cracking in cast Haynes 282, but firmly establishing tendencies for it will require a more focused, detailed study.

3.1.5 Weld Deposit Results

The photographs in Figure 15 show the full depth of the cross-sectioned weld before and after final heat treatment. The weld deposit is characterized by the variations of microstructure normally associated with deposition of successive weld beads. Otherwise, it appears to be of high quality with no visible indications of physical defects like porosity, lack-of-fusion defects, cracking, or entrapment of extraneous materials. Defects in the cast base metal are also visible.

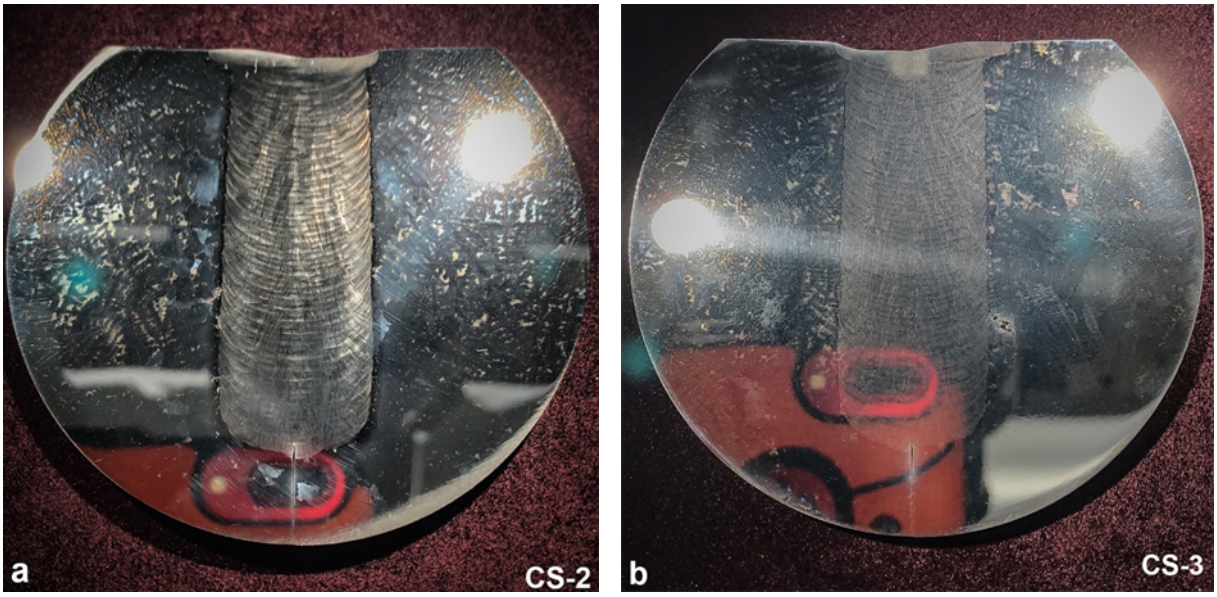

Figure 15: Photographs of full-section weld deposit (a) as-welded, and (b) after post-weld strengthening heat treatment

Optical micrographs taken in the weld deposit show its microstructure before, Figure 16(a), and after, Figure 16(b), the final heat treatment. The dendritic structure with secondary dendrite arm spacing in the 5-8 μm range is clearly visible before heat treatment. Interdendritic regions etched much darker after heat treatment, presumably related to precipitation in those locations. Well defined grain boundaries are also visible after heat treatment. The light etching band in the lower half of Figure 16 is associated with the boundary between successive weld beads. Heating from deposition of the upper bead could promote a local variation of precipitation and encourage a limited amount of elemental distribution. Epitaxial growth of grains from the lower bead into the upper one is also apparent.

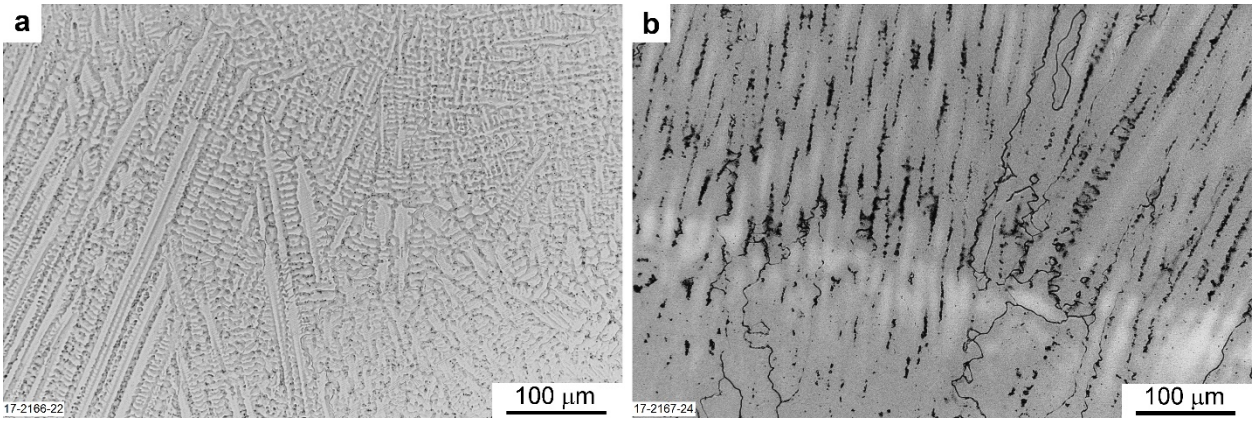

Figure 16: Optical micrographs of the weld deposit before (a) and after (b) post-weld strengthening heat treatment

The series of optical micrographs presented as Figure 17 provide a more detailed view of the weld deposit after post-weld heat treatment. This specimen was prepared for examination in the SEM. The dark features in the micrographs are the interdendritic regions.

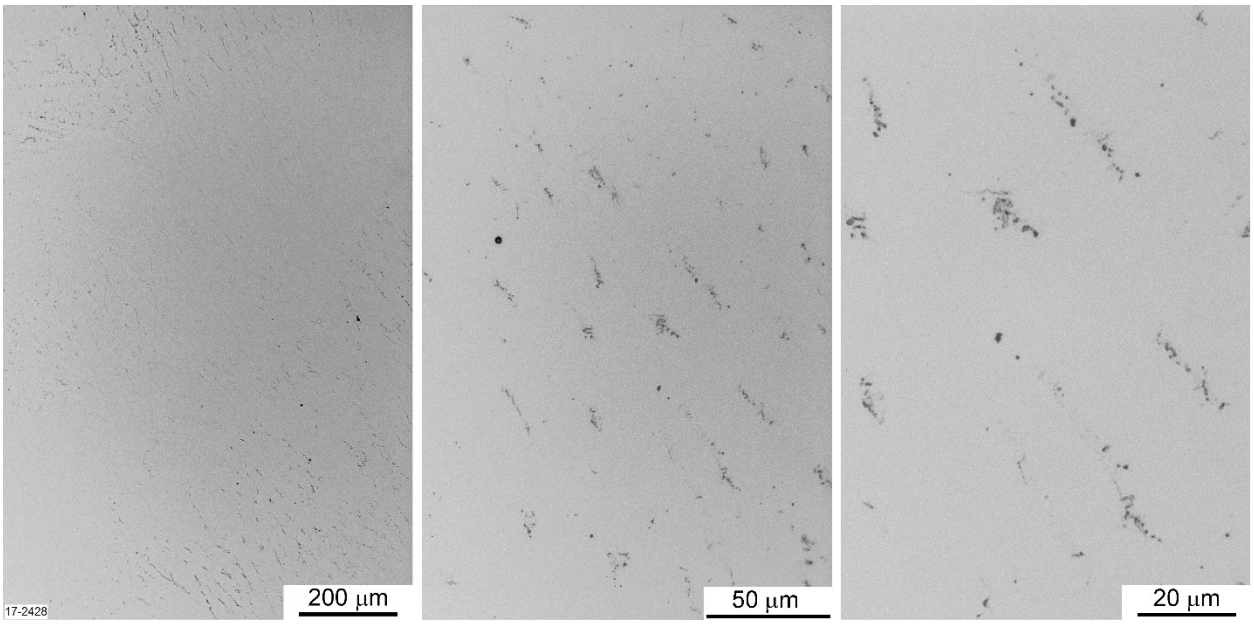

Figure 17: Optical micrographs of weld deposit after post-weld strengthening heat treatment

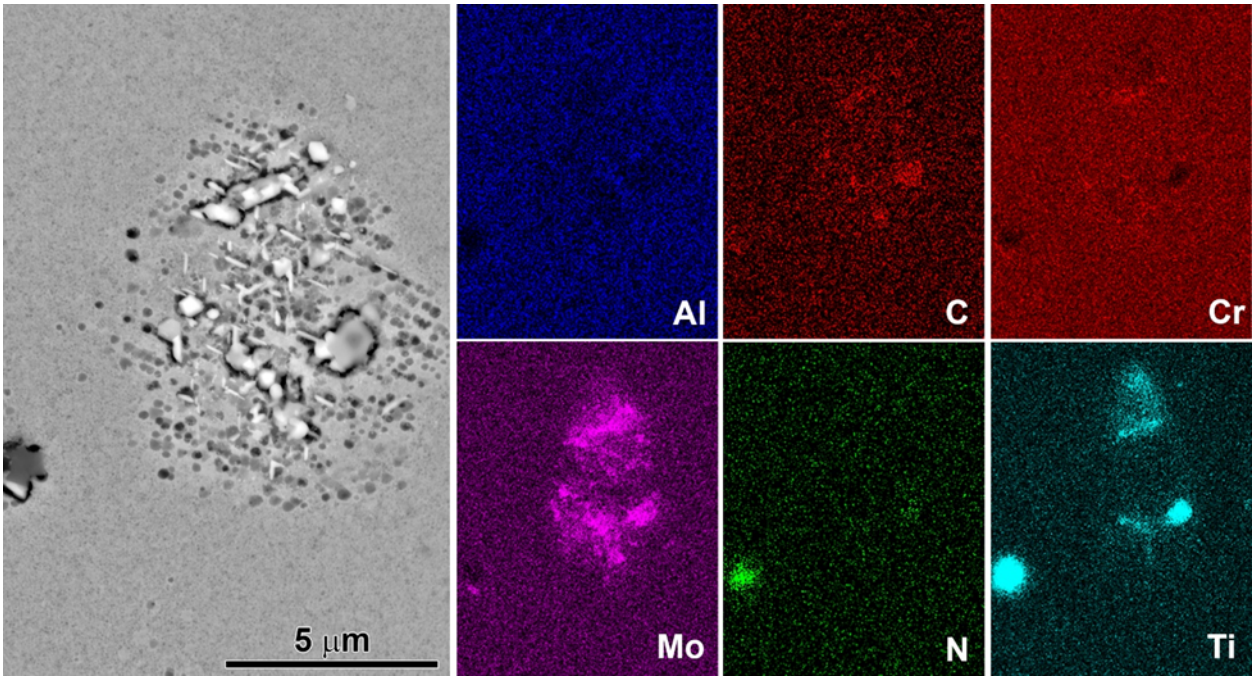

Figure 18: SEM micrograph and analysis results from interdendritic region of weld deposit after post-weld strengthening heat treatment

The results from SEM examination of an interdendritic region in the weld deposit are shown in Figure 18, where particles ranging in size from submicron to several microns in major dimension were found. The chemical analysis results show that Mo is distributed throughout the group of particles. Judging from their contrast, many particles have relatively high Mo concentrations, including small particles that present as rod-shapes on this planar surface. These could be the type of particles imaged in Figure 8. A few of the

larger particles appear to have the contrast, contrast gradation, and chemical composition characteristics of the MC carbide and nitride phases found throughout the base metal. There is also an indication of the presence of small particles enriched in Cr, similar to those shown in Figure 7. The small spherical particles distributed mainly around this grouping are likely the γ′ phase.

3.1.6 Weld Deposit Discussion

From a practical perspective, nothing about this weld deposit raises any concerns about the ability to produce high quality weld deposits with the Haynes 282 alloy. No physical defects of any kind were found in the weld deposit. This is consistent with related work [8] on welding cast metal. A more recent study [23] showed that weld deposits are susceptible to solidification cracking. However, that behavior could be related to welding practice rather than the intrinsic characteristics of the alloy.

Some details about the solidification behavior of Haynes 282 were analyzed by Bechetti et al [24]. This work showed that Mo partitions strongly to interdendritic regions, and that concentrations of Cr and Ti there will also be elevated. Further analysis of solidification sequence indicated that intermetallic phases such as μ and σ also are likely to occur in interdendritic regions as solidification ends. The SEM results presented in Figure 18 are generally consistent with those predictions. Mo and much lower amounts of Cr and Ti, all were found elevated interdendritically. Identifying the phases found at these locations will required more detailed examination.

3.2 PROPERTIES

3.2.1 Hardness Results

Vickers microhardness testing was used for an initial assessment of the weldment properties. The hardness testing was done on lightly etched specimens using an indenter load of 200 g. The hardness indents were automatically arranged in 4-mm-x-8-mm arrays with indent spacing of 200 μm. This produced 861 total indents. Application and measurement of the indents was done automatically. The arrays were positioned so that the 8-mm array length was approximately normal to and centered about the weld-metal/base-metal interface.

The results from hardness testing are presented in Figure 19. The upper portion of each figure is an optical micrograph showing the arrays after the indentation procedure, and the lower portion is an image plot of the data showing its distribution around the weld deposit/base metal fusion boundary. The approximate location of the fusion boundary is also shown on the hardness image plots. Average hardness values were determined using the leftmost 5 x 21 indent arrays for the weld deposit and the rightmost ones for base metal. In the as-welded condition, Figure 19(a), the weld deposit hardness is 341 ± 16, and the base metal hardness is 355 ± 10. Using a 3 x 21 array, the hardness was estimated as 321 ± 26 in the narrow, light-etching region in the base metal adjacent to the fusion boundary.

Figure 19(b) shows that the hardness increased everywhere after the post-weld heat treatment. The base metal experienced an increase up to an average value of 370 ± 13. In contrast, heat treatment increased the hardness of the weld deposit to 399 ± 12. The hardness of the near heat-affected zone adjacent to the fusion boundary increased to 367 ± 18, just slightly below the average base metal value.

The hardness data are also plotted in Figure 20 as line traverses across weld metal, heat-affected zone, and base metal. Because the arrays are composed of stacks of 21-line traverses these were averaged to illustrate the scatter. Figure 20 further highlights the increases of hardness induced by post-weld heat treatment. It also confirms that a region of slightly depressed hardness persisted adjacent to the fusion boundary after the heat treatment.

3.2.2 Hardness Discussion

Before welding, the base metal was solution treated at 1150°C, a temperature high enough to dissolve γ′ strengthening precipitates. However, the cooling rate after solution treatment was in the range of several °C/min, slow enough for some reprecipitation of γ′ to occur [19]. In comparison, temperatures due to local heating from welding would have approached the solidus, around 1261°C, with cooling at a relatively high rate, perhaps on the order of 100°C/min. From this, it is plausible that reprecipitation of γ′ in the near heat-affected zone was suppressed relative to what might occur when cooling from solution treatment. This scenario is consistent with reduced hardness in the near heat-affected zone as Figure 19 and Figure 20 show. These figures also show there was a slight increase of hardness in the base metal beyond this softer zone. This behavior is consistent with a strain aging response as previously suggested.

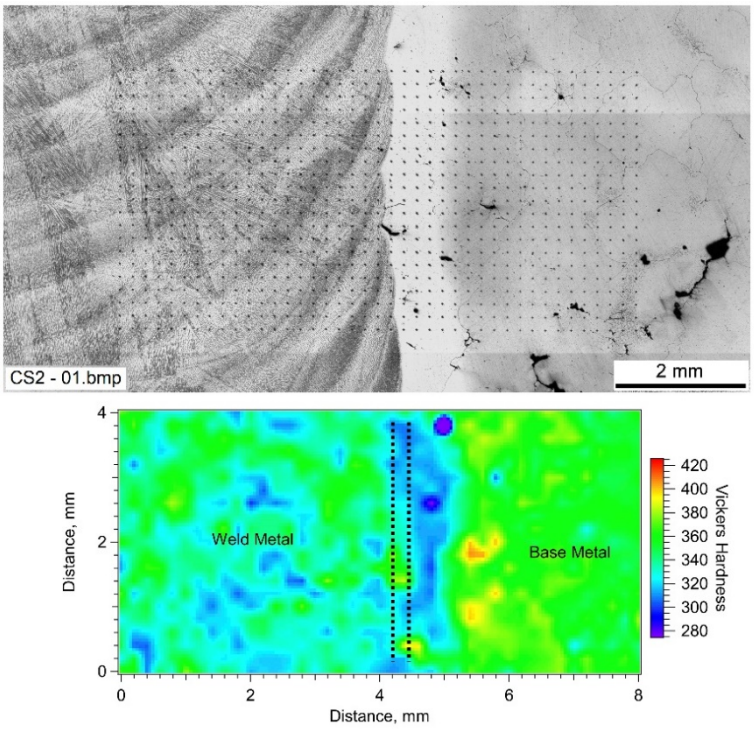

(a)

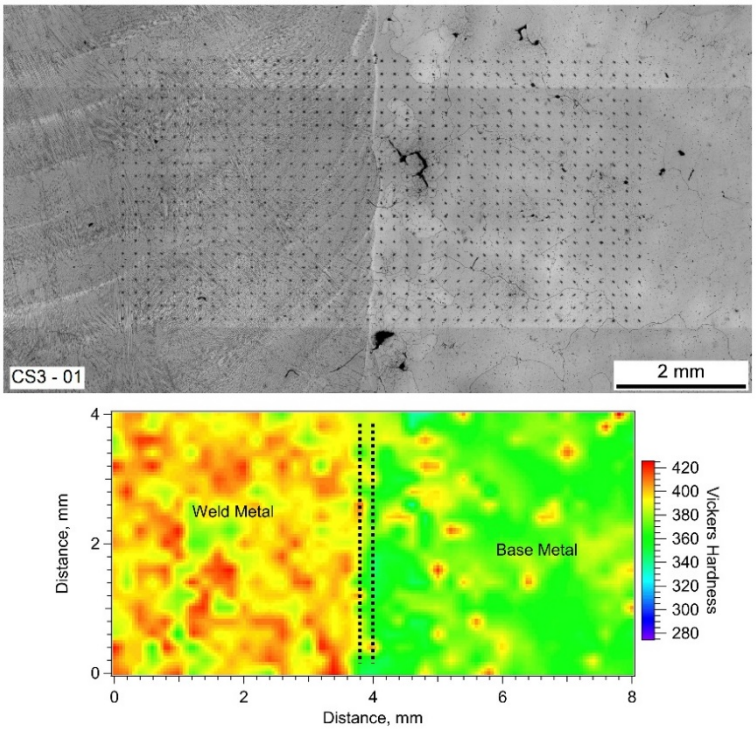

(b)

Figure 19: Hardness distributions: (a) as welded condition with solution-treated base metal; (b) and after post-weld strengthening heat treatment

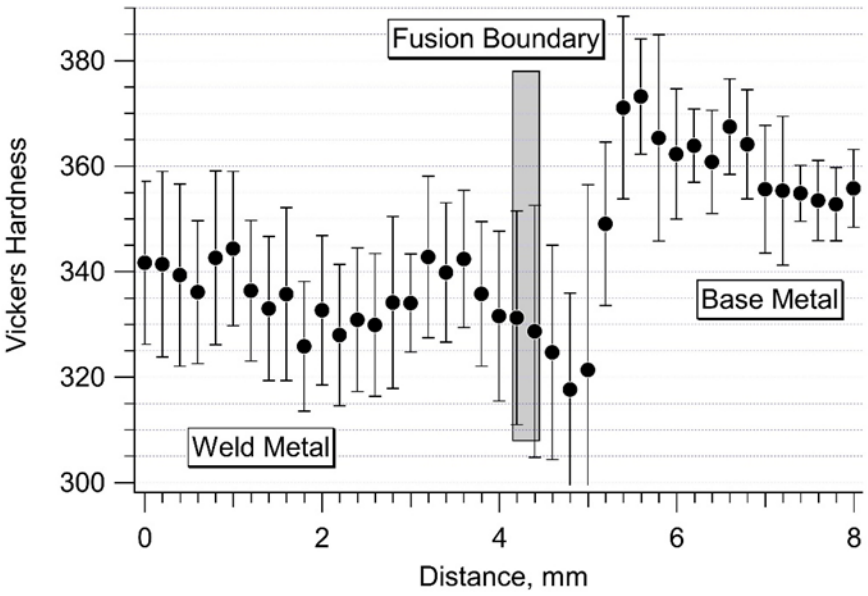

(a)

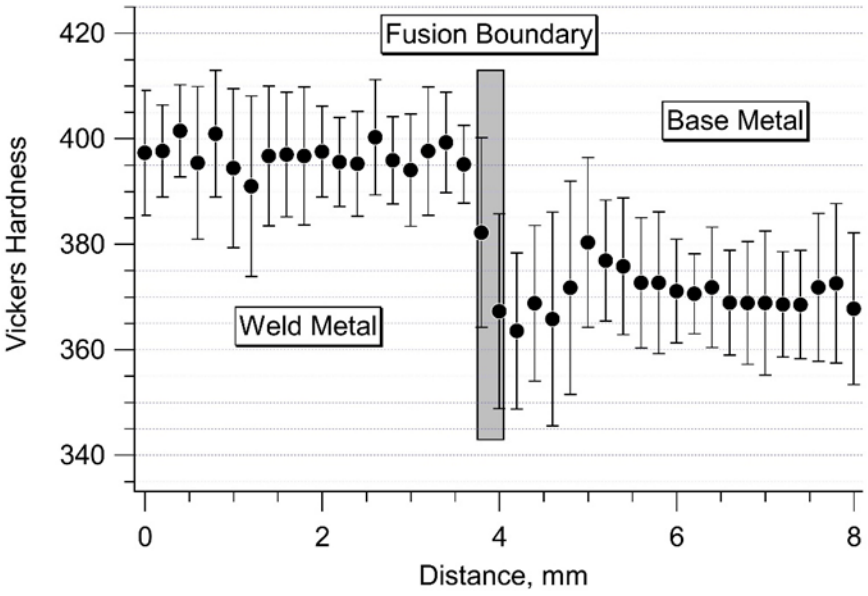

(b)

Figure 20: Hardness traverse plots: (a) as-weld condition with solution-treated base metal; and, (b) after post-weld strengthening heat treatment

The hardness increase in the weld deposit compared to the base metal after post-weld heat treatment could be caused by its higher Al concentration and low concentrations of C, Table 1. The higher Al concentration in the weld deposit would slightly increase the amount of γ′. The lower C concentration, for instance, would reduce the amount of Ti precipitating in Ti-rich MC phases. This would permit more Ti to participate in forming γ′. The microstructure observations are consistent with the weld deposit having a lower amount of MC phases compared to the base metal.

Figure 19(b) and Figure 20(b) indicate that hardness gradients in the heat-affected zone were nearly eliminated by the post-weld strengthening heat treatment. These figures also indicate there is no clear effect of local recrystallization, Figure 11(b), on the hardness.

3.2.3 Strength Testing

A set of machined specimens was selected at random from the group of 30 for tensile testing. Afterwards, but before stress-rupture testing, the general condition of the remaining specimens was assessed by dye-penetrant inspection. The inspected specimens were grouped into three categories based on visual defect size indications of (1) none to 0.4 mm maximum, (2) 0.4-1.6 mm, and, (3) over 1.6 mm. Specimens in category 1 were used for initial stress-rupture testing with the remainder held in reserve for subsequent testing.

3.2.3.1 Tensile Strength

The results from tensile testing of cross-weld specimens are tabulated in Table 2. The variation of yield strength with test temperature is plotted in Figure 21 where the cross-weld results are compared to those of Haynes International for wrought metal [25], and those from base metal testing at a different location, designated as, H, in the original 7,700 kg cast body [8]. Over the temperature range shown in Figure 21, the yield strength of the cast base metal ranges from about 80-85% of wrought metal reference values. The cross-weld values were further reduced to the range of about 80% of the location H base metal values or 60-70% of reference values. A similar difference between the tensile behavior of cast and wrought 282 alloy was found by Kim and coworkers [26].

No detailed fractography was done on the broken cross-weld specimens but most failure locations were clearly in the cast base metal. Even those specimens designated in Table 2 as failing in the heat-affected zone will need closer examination to determine whether microstructure there was specifically responsible for failure. One factor that would contribute to lower strength in the cross-weld specimens is the presence of casting defects. No effort was made to specifically characterize the overall defect condition of the original large casting, but there is no reason to assume defects were uniformly distributed. The location where stock sourced for making the weld was taken, near a riser, appeared to contain a relatively high concentration of casting defects compared to the H location [8] used for the cast base metal values plotted in Figure 21.

Lastly, there is no compelling evidence that the effects from welding created any conditions directly leading to reduced yield strength values. Considering its hardness characteristics, relatively small grain size, and generally defect-free state, the weld deposit can reasonably be assumed to have higher strength and ductility values than the cast base metal.

Table 2: Tensile Data for Cross Weld Specimens of Cast Haynes 282 Alloy

ID	T, °C	YS, MPa	UTS, MPa	Elong., %	ROA, %	Failure
SB18	22	497	550	0.5	---	Base
SB28	371	474	474	0.23	---	Base
SB7	704	509	510	1.03	---	Base
SB9	760	505	507	1.15	---	HAZ
SB30	816	76	76	0.3	---	HAZ
SB12	816	454	468	2.2	2.8	Base

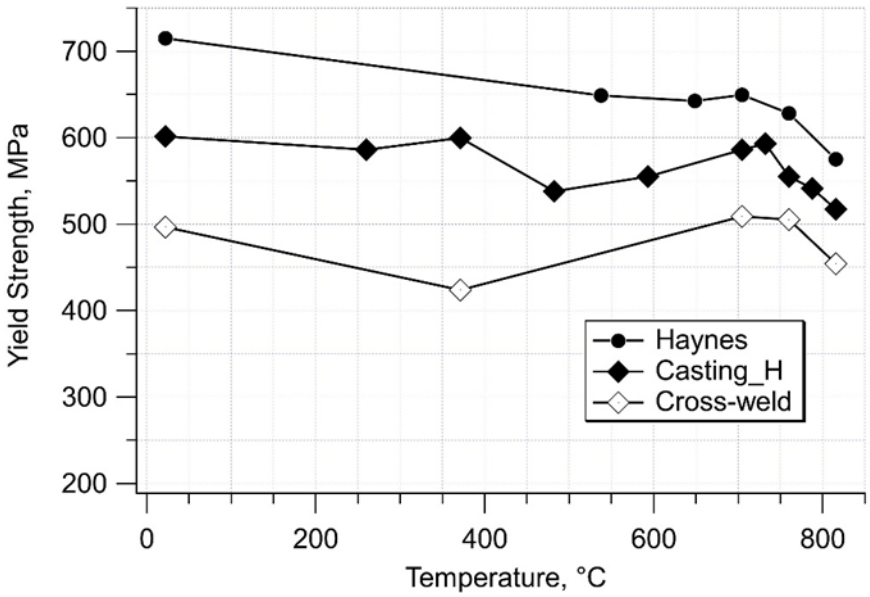

Figure 21: Comparison of yield strength for base metal and cross-weld test specimens

3.2.3.2 Stress-rupture

The results from stress-rupture testing of cross-weld specimens are tabulated in Table 3. The variation of Larson-Miller parameter with applied stress is shown in Figure 22, where the solid line represents the reference results from testing wrought base metal [7,8,25]. Also included on the plot are results from tests of cast base metal [27], and cross-weld specimens of wrought base metal [7]. The dotted line in Figure 22 represents the base metal reference data with stress values reduced by 20%. The bracketed values for life in Table 3 indicate specimens still in-test as of 07/14/2020. Just as for the tension tests, the failure locations of the cross-weld specimens were in the cast base metal. This indicates that the rupture strength of the weld deposit exceeds that of the cast base metal and that the intrinsic strength of the cast base metal controlled failure. It further suggests that heat-affected zone microcracking and localized recrystallization had no significant effect on cross-weld rupture strength.

Figure 22 shows that the cross-weld rupture strength is essentially identical for cast and wrought base metal. Furthermore, the rupture strengths of cross-weld specimens as well as cast base metal specimens were well within 80% of the rupture strength of wrought base metal reference results.

Table 3: Creep Rupture Data for Cross Weld Specimens of Cast Haynes 282 Alloy

ID	Test	Stress, MPa	T, °C	Life, h	Elong., %	ROA, %
SB2	33611	336	704	1744.4	4.0	41.6
SB5	33838	324	704	6118	4.9	29.8
SB3	33489	256	760	2454.6	4.2	37.7
SB13	33836	198	760	6470	5.2	8.8
SB6	33612	136	816	3218.2	3.5	5.9
SB4	34759	303	704	[6293]		
SB14	34758	179	760	[6293]		
SB26	38361	110	816	[3509]		
SB15	33837	90	816	[14642]		

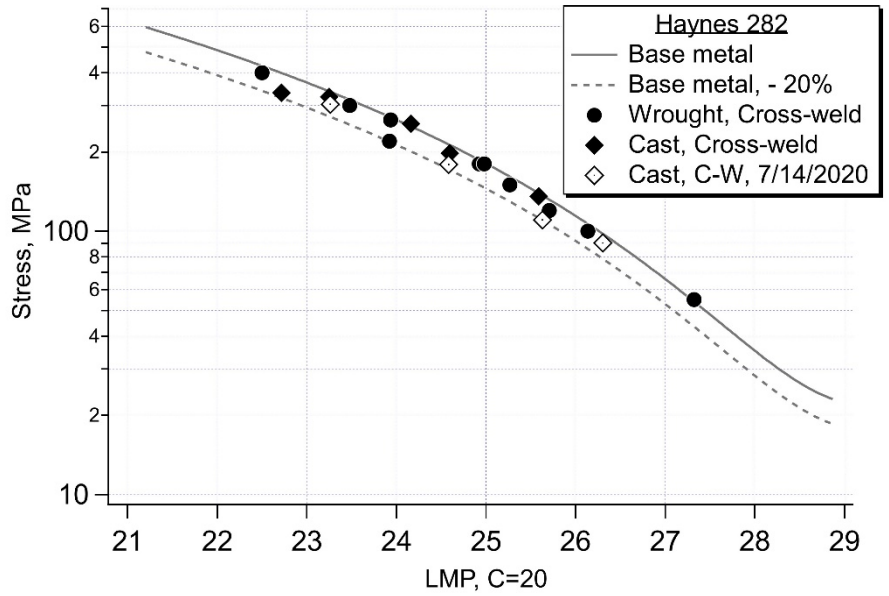

Figure 22: Larson-Miller plot of cross-weld stress-rupture results. Open symbols represent on-going tests.

Considering the condition of the cast base metal with regard to casting defects and microcracking, its performance relative to wrought metal in stress-rupture testing may be surprising. In terms of precipitation, the microstructure of the wrought base metal is considered optimized for creep strength [9,10,28]. However, besides uniform dispersions of γ′ and carbides, increasing grain size can also benefit performance in creep conditions [29]. The state of the cast base metal relative to precipitation of γ′ is not well characterized, but its large grains would tend to be an advantage in creep loading over wrought metal with much smaller grain size. This advantage of larger grains derives from the much smaller number of grain boundary triple points where nucleation of creep cracks is favored. However, any grain size advantage of the cast base metal would be offset to some extent by the presence of defects and microcracking that would eliminate the time needed for crack nucleation in creep loading conditions.

Another potential advantage of the cast metal over wrought metal is related to the distribution of large carbides along its grain boundaries. There are many carbides on grain boundaries with major dimension ≥ 50 μm. As well as much smaller, uniformly distributed carbides, ones in this large size range can benefit creep properties [30]. In any event, it is clear that the presence of defects in the cast base metal does not significantly decrease its rupture strength compared to wrought base metal. Similarly, the intrinsic

strength of the cast base metal is high enough to offset any effects of heat-affected zone issues in tests of cross-weld specimens.

4. SUMMARY

A 50-mm deep gas-tungsten arc weld was made in a ring section of a 7,700-kg casting of Haynes 282 alloy. Spooled 1.14-mm-diameter welding wire, purchased from Haynes, was used for the welding. A total of 104 weld beads were used to fill the joint groove. During welding, numerous cracks were observed in the machined face of the base metal weld groove, but welding continued to completion. After welding, various specimens were cut from the weldment for metallographic analysis and testing. Some of specimens used for metallography were maintained in the as-welded condition. Others were given the recommended strengthening heat treatment of 2 h at 1010°C followed by 8 h at 788°C. The cross-weld specimens for tension and stress-rupture testing were given the same heat treatment after machining.

The chemical compositions of both the cast base metal and the weld deposit agreed with that of UNS N07208, the ASTM specification for wrought Haynes 282.

The microstructure of the cast base metal was characterized by large grain size. Average grain size was not estimated, but grains exceeding several millimeters in major dimension could be easily seen on smooth, cut, or machined surfaces without the aid of magnification. Grain boundaries and interdendritic regions were outlined with large second-phase particles. Most of the particles were MC phase with variable chemical composition of (Mo,Ti)(C,N). Many of these particles exceeded 50 μm in major dimension. Large particles enriched in Mo and Si were also found on grain boundaries.

The weld heat-affected zone microstructure was characterized by microcracking and localized recrystallization. Direct evidence of the likely source of the microcracking could not be identified. The localized recrystallization was found only after the strengthening heat treatment.

The weld deposit was of high quality with no visible indications of physical defects like porosity, lack-of-fusion defects, cracking, or entrapment of extraneous materials. Interdendritic regions in the weld deposit contained an MC phase similar to that in the base metal but much smaller, ranging up to a few microns in average size. Other particles in the interdendritic regions were submicron in average size and generally enriched with Mo.

In the as-welded condition, average Vickers hardness values were 341 ± 16 in the weld deposit, 355 ± 10 in the base metal, and 321 ± 26 in a narrow, light-etching region immediately adjacent to the weld fusion line in the heat-affected zone. After the strengthening heat treatment, the base metal experienced a hardness increase up to an average value of 370 ± 13. In contrast, heat treatment increased the hardness of the weld deposit to 399 ± 12. The hardness of the near heat-affected zone adjacent to the fusion boundary was increased to 367 ± 18.

The results from tensile testing of cross-weld specimens up to 816°C showed that their strengths were about 80% of the yield strength determined from testing the base metal at another location of the original 7,700 kg casting. The cross-weld values were about 60-70% of reference values for wrought 282 base metal. Nevertheless, failure locations for the cross-weld specimens were in base metal rather than the weld deposit or heat-affected zone. There is no evidence that the effects from welding created any conditions directly leading to reduced yield strength values.

The rupture strength of cross-weld specimens is being evaluated at temperatures of 704°C, 760°C, and 816°C, and stress levels of 90-336 MPa. To date, ruptured specimens failed in base metal within 20% of wrought base metal reference data.

5. ACKNOWLEDGEMENT

This research was sponsored at the Oak Ridge National Laboratory by the U.S. Department of Energy, Office of Fossil Energy, under Contract DE-AC05-00OR22725 with UT-Battelle, LLC. Significant contributions to this work were made by Alan Frederick, Tom Geer, Doug Kyle, Tracie Lowe, and Jeremy Moser. Their support was critical to coordinating and completing numerous technical activities, testing, and analyses. Technical discussions with Michael Haines of University of Tennessee were appreciated. Wei Tang and Peter Tortorelli reviewed the manuscript for technical content and provided many thoughtful comments.

6. REFERENCES

1. "The U.S. Coal Sector. Recent and continuing challenges," H. Gruenspecht, Paper 6, January 2019, The Brookings Institution, Washington, D.C., https://www.brookings.edu/

2. T. Wall et al., "An overview on oxyfuel coal combustion—State of the art research and technology development," Chemical Engineering Research and Design, Volume 87, 2009, 1003-1016

3. D. I. Barnes, "Understanding pulverised coal, biomass and waste combustion - A brief overview," Applied Thermal Engineering, Volume 74, 2015, 89-95

4. R. Viswanathan and W. Bakker, "Materials for Ultrasupercritical Coal Power Plants—Boiler Materials: Part 1," Journal of Materials Engineering and Performance," Volume 10, Issue 1, 2001, 81-95

5. R. Viswanathan and W. Bakker, "Materials for Ultrasupercritical Coal Power Plants—Turbine Materials: Part II," Journal of Materials Engineering and Performance," Volume 10, Issue 1, 2001, 96-101

6. R. Viswanathan, J.F. Henry, J. Tanzosh, G. Stanko, J. Shingledecker, B. Vitalis, and R. Purgert, "U.S. Program on Materials Technology for Ultra-Supercritical Coal Power Plants," Journal of Materials Engineering and Performance," Volume 14, Issue 3, 2005, 281-292

7. R. Purgert, J. Shingledecker, R. Ganta, J. Pschirer, P. Weitzel, J. Sarver, B. Vitalis, M. Gagliano, G. Stanko, and P. Tortorelli, Boiler Materials for Ultra Supercritical Coal Power Plants, Final Technical Report, December 2015, DOI 10.2172-1346714

8. R. Purgert, J. Shingledecker, D. Saha, M. Thangirala, G. Booras, J. Powers, C. Riley, and H. Hendrix, Materials for Advanced Ultrasupercritical Steam Turbines, Final Technical Report, December 2015, DOI 10.2172-1243058

9. L. M. Pike and H. L. Flower, "Gas Turbine Superalloy with Improved Fabricability," Advanced Materials and Processes, June 2006, 39-42

10. "DEVELOPMENT OF A FABRICABLE GAMMA-PRIME (γ') STRENGTHENED SUPERALLOY," L. M. Pike, 191-200, Superalloys 2008, edited by R. C. Reed, K. A. Green, P. Caron, T. P. Gabb, M. G. Fahrmann, E. S. Huron, and S. A. Woodard, TMS, 2008

11. P.D. Jablonski, J.A. Hawk, C.J. Cowan, and P.J. Maziasz, JOM, Volume 64, No. 2, 2012, pp. 271-279

12. JMatPro® Practical Software for Materials Properties, Ni Alloy database, Sente Software Ltd., https://www.sentesoftware.co.uk/jmatpro

13. Jeffrey A. Hawk, Tian-Le Cheng, John S. Sears, Paul D. Jablonski, and You-Hai Wen, Journal of Materials Engineering and Performance, Volume 24(11) November 2015, pp. 4171-4181

14. P.J. Ennis, A. Strang, S.P. Gill, G.M. McColvin, and H.V. Atkinson: Energy Mater., 2012, vol. 4, pp. 184–88.

15. H. Matysiak et al., Materials 2013, 6, 5016-5037; doi:10.3390/ma6115016

16. YANG, Y. et al, 2014. Microstructural evolution in cast Haynes 282 for applications in advanced power plants. IN: Gandy, D. and Shingledecker, J. (eds). Advances in Materials Technology for Fossil Power Plants: Proceedings from the Seventh International Conference (EPRI 2013), 22nd-25th October 2013, Waikoloa, Hawaii, USA. ASM International, pp. 143 - 154.

17. L.O. Osoba, R.G. Ding, and O.A. Ojo, Metallurgical and Materials Transactions A, Volume 43A, November 2012, pp. 4281-4295

18. J. Andersson, G. Sjöberg, and M. Chaturvedi, "Hot Ductility Study of HAYNES® 282® Superalloy," 7th International Symposium on Superalloy 718 and Derivatives, edited by E.A. Ott, J.R. Groh, A. Banik, I. Dempster, T.P. Gabb, R. Helmink, X. Liu, A. Mitchell, G.P. Sjörberg, and A. Wusatowska-Sarnek, TMS, 2010, pp. 539-554

19. M.G. Fahrmann and D.A. Metzler, JOM, Vol. 68, No. 11, 2016, DOI: 10.1007/s11837-016-2097-5

20. Welding Metallurgy and Weldability of Nickel-Base Alloys, J.N. DuPont, J.C. Lippold, and S.D. Kiser, John Wiley & Sons, Hoboken, New Jersey, 2009, pp. 223-235

21. L.O. Osoba and O.A. Ojo, Materials Science and Technology, Volume 28(4), 2012, pp. 431-436

22. L.O. Osoba, A.K. Khan, and O.A. Ojo, Metallurgical and Materials Transactions A, Volume 48A, April 2017, pp. 1540-1543

23. F. Hanning and J. Andersson, Weld World, 2018 volume 62, pp. 39–45

24. D.H. Bechetti, J.N. DuPont, J.A. Siefert, and J.P. Shingledecker, Metallurgical and Materials Transactions A, Volume 47A, September 2016, pp. 4502-4518

25. Haynes® 282® alloy, copyright 2017 Haynes International, H-3173B, https://haynesintl.com

26. Y.-J. Kim, J.-H. Park, and Y.-S. Ahn, Advances in Materials Science and Engineering, Volume 2018, Article ID 2048959, 7 pages, https://doi.org/10.1155/2018/2048959

27. P.J. Maziasz, J. Moser, K. Unocic, Y. Yang, D. Purdy, and P.D. Jablonski, "Tensile, Creep and Microstructural Behavior of Welded Cast Haynes 282 Alloy for A-USC Steam Turbine Casing Applications," pp. 703-714 in Advances in Materials Technology for Fossil Power Plants, edited by J. Parker, J. Shingledecker, and J. Siefert, Proceedings from the Eighth International Conference, October

11–14, 2016, Albufeira, Algarve, Portugal, published by ASM International®, Materials Park, Ohio 44073-0002, www.asminternational.org

28. D.L. Klarstrom, L.M. Pike, and V.R. Ishwar, Procedia Engineering, volume 55, 2013, pp. 221-225

29. C.D. Liu, Y.F. Han, M.G. Yan, and M.C. Chaturvedi, "Creep Crack Growth Behavior of Alloy 718," pp. 537-548 in SuperAlloys 718, 625, and Various Derivatives, edited by E.A. Loria, The Minerals, Metals, and Materials Society, 1991

30. J. Rösler and A.G. Evans, Materials Science and Engineering, volume A153, 1992, pp. 438-443

APPENDIX A.
NARROW GROOVE GTA WELDING EVALUATION
JOINING OF CAST HAYNES 282 WITH HAYNES 282 RTW WIRE

Adobe Acrobat
Document

APPENDIX B.
SPECIMEN REMOVAL AND POST WELD HEAT TREATMENT OF NARROW GROOVE WELDMENT JOINING CAST HAYNES 282 WITH 282 RTW W

Adobe Acrobat
Document